Engineering Journal issn: 0125-8281

Article

Influence of pH-Driven Synthesis on the Performance of NiO as a Hole Transport Layer in Perovskite Solar Cells

Subathra Muniandy[1,a,*], Muhammad Idzdihar Bin Idris[1,b], Zul Atfyi Fauzan Bin Mohammed Napiah[1,c], Nicolas Sii Tiing Kie[1,d], Zarina Baharudin[1,e], and Marzaini Rashid[2,f]

1 Faculty of Electronic and Computer Technology and Engineering, Universiti Teknikal Malaysia Melaka, Melaka, Malaysia
2 School of Physics, Universiti Sains Malaysia, Penang, Malaysia
E-mail: [a,*]p122410006@student.utem.edu.my (Corresponding author), [b]idzdihar@utem.edu.my, [c]zulatfyi@utem.edu.my, [d]nikcoand@gmail.com, [e]zarina@utem.edu.my, [f]marzaini@usm.my

Abstract. The hole transporting layers (HTL) is a fundamental layer in perovskite solar cells (PSCs) structures. Generally HTL composed of PEDOT:PSS material that has a drawback of a high cost, lengthy synthesis process, and insufficient stability. Nickel oxide (NiO) as an inorganic HTL has been emphasized in PSCs owing to low cost, solution-based processing and the good band alignment. This study presents the effect of synthesized NiO at different pH values (9-12) using a spin-coating method annealed at 500 ºC, 600 ºC, and 700 ºC. The in-depth characterization of the synthesized NiO was executed by XRD, SEM and FTIR to investigate their structural, element composition and morphological. According to XRD findings, all the prominent diffraction peaks of NiO at 37.2º, 43.36º, 63.04º, and 75.51º were observed only in pH 11. The SEM revealed the surface morphology of pH 11 have good coverage with less agglomeration of particles as compared to other pH values. A strong absorption peak was observed in FTIR analysis (400cm^{-1} to 600cm^{-1}), ascribed to the presence of NiO vibration. Based on these findings, NiO produced at pH 11 annealed at 700 ºC exhibited promising characteristics, suitable for HTL in PSCs.

Keywords: Hole transporting layer, nickel oxide, spin coating, pH values.

ENGINEERING JOURNAL Volume 29 Issue 4
Received 4 December 2024
Accepted 8 April 2025
Published 30 April 2025
Online at https://engj.org/
DOI:10.4186/ej.2025.29.4.23

1. Introduction

Today's economy offers a vast range of photovoltaic cell innovations made of various substances, and an even larger proportion would be useful in the future. Depending on the raw product being used and the degree of market development, photovoltaic cell development is split into three generations [1]. The first-wave photovoltaic systems use crystalline silicon (c-Si) technologies, second wave, photovoltaic systems employ thin-film solar cell techniques, whereas third-wave photovoltaic systems comprise organic photovoltaics inventions, perovskite solar cells (PSCs), and dye-sensitized solar cells (DSSC), polymer PV solar cells, and hybrid solar cells [2]. Among the various types of solar cells, PSCs are the most statement of the intended route to sunlight harvesting. PSCs are an important topic in renewable energy resources due to their exceptional capacity to convert solar power towards electrical with high power conversion efficiency [3]. Although poly(3,4-ethylenedioxythiophene) polystyrene sulfonate (PEDOT:PSS) is a commercialized standard hole transport material, it is proved that the PEDOT:PSS devices have insufficient long-term stability, due to intrinsic problems. Besides that, PEDOT:PSS films suffer from extreme hygroscopic nature and acidity, along with a substantial compromise in their conductivity due to the presence of PSS counter anion which is non-conductive. This is especially critical in inverted architectures where the perovskite layer is exposed to the HTM. PEDOT:PSS films are not fully transparent in the visible range, which can limit the amount of light reaching the perovskite layer. This can result in reduced overall efficiency of the solar cell. Besides that, achieving good interface engineering between PEDOT:PSS and the perovskite layer can be challenging [4]. PEDOT:PSS solutions have a tendency to form aggregates or show inhomogeneity during spin coating, affecting the overall film quality. The choice of substrate can influence the performance of the spin-coated PEDOT:PSS film. As a result, various inorganic hole transport materials, such as Copper(I) thiocyanate (CuSCN), Copper(I) iodide (CuI), Copper(I) oxide (Cu2O), Copper(II) oxide (CuO), Cobalt(II) oxide (CoO), and NiO, have been investigated for PSCs [5]–[7]. Extensive experimentation has been done on NiO-based PSCs in specific. NiO is among the most effective hole-transporting materials for PSCs [6]. As a result, the mechanism of NiO as HTM was explored in this project to improve the effectiveness of PSCs.

In this work, an experimental study focus on the influence of four different pH levels (9, 10, 11 and 12) of NiO thin film as HTL was carried out by spin coating deposition for two separate layers, top (supernatant) and bottom (precipitate) obtained through the synthesis process which were thermally treated at three different temperature (500°C, 600°C and 700°C). The development of low-cost, high-throughput, and customizable large-area PSCs requires solution-processable HTMs. The goal of this research is to synthesize NiO using a low-cost, solution-based processing method. Spin coating provides excellent control over the thickness and uniformity of the deposited NiO film. The spinning action ensures a homogeneous distribution of the precursor solution, leading to uniform coverage over the substrate. This uniformity is crucial for the performance of thin-film devices, such as solar cells and sensors. Spin coating is a relatively simple and cost-effective deposition technique. The simplicity and scalability of the spin coating process make it conducive to industrial-scale production. This is advantageous when transitioning from laboratory-scale synthesis to commercial applications.

2. Methodology

2.1. Materials

Nickel acetate tetrahydrate, 98% ($Ni(CH_3COO)_2.4(H_2O)$), was bought from Sigma Aldrich. Besides that, ethanol (C_2H_5OH) (purity, 95%), potassium hydroxide (KOH), and isopropyl alcohol, (IPA) (C_3H_8O) were purchased from Chemiz (M) Sdn Bhd. Deionized water (H_2O) was used to prepare all aqueous solutions. All chemicals with high purity were used without any further purification.

2.2. Substrate Preparation

Substrate preparation is a key step that could be employed to control experimental factors such as the size of a PSC's active region. Substrate preparation corresponds to the procedures that must be followed to make sure that a material was ready for use before a protective coating or other substance were applied to its surface. The purpose of substrate preparation is to guarantee that contaminants from the surface, such as dust, paint, and dirt, are removed therefore the substrate can be coated without being affected. This procedure significantly enhances the coating's adherence to the substrate, improving coating quality and dependability. The method involves cutting and cleaning, an ITO substrate. Initially, the ITO substrate was sliced into 2.5 x 2.5 cm squares using a diamond cutter and cleaned to eliminate dirt and stains from the surfaces. ITO substrates and beakers were initially washed with soaps and then rinsed with IPA, ethanol, and deionized water, correspondingly, while being sonicated for approximately 30 minutes in ultrasonication. Substrates and beakers were placed in an oven to dry.

2.3. Synthesis of NiO

NiO nanoparticles were synthesized according to the previous report [8], [9]. Briefly, 0.622g nickel acetate tetrahydrate was dissolved in the mixture of ethanol (15 ml) and IPA (10 ml). The mixed solution was then magnetically stirred under an ambient atmosphere to obtain a clear solution. The stirring of solutions enhanced the dissolving process and accelerated the speed of

chemical reactions. The pH of the solution at the beginning was at a value of 7. The pH of the solution was then obtained at the value of 9 at room temperature after adding potassium hydroxide dropwise as illustrated in Fig. 1. The step was repeated for different pH values (9-12). The role of potassium hydroxide acts as a stabilizer to adjust the pH of solutions and as a thickening agent. Next, the solution was then stirred for 2 hours at 60 °C using a heating magnetic stirrer. The mixture was slowly cooled to room temperature. The top part (supernatant) and the bottom part (precipitate) were refined by rinsing with ethanol over five times to eliminate residual chemicals. The resultant gel was gathered for coatings and characterization purposes.

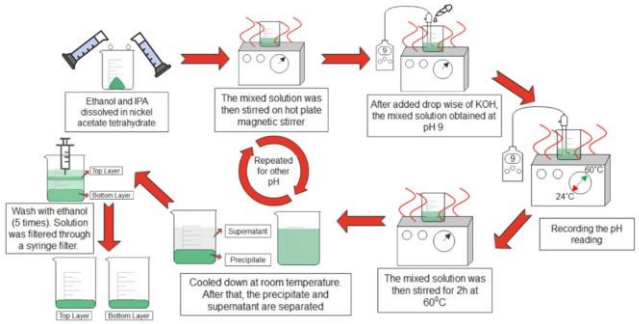

Fig. 1. The detailed synthesis of the NiO procedure.

2.4. Deposition of NiO

NiO coating sol-gel obtained from the synthesis procedure was deposited onto a glass substrate by using the spin coating technique. First, the obtained NiO sol-gel solution was dropped onto a microscope glass substrate and then coated at the acceleration of 3000 rpm for 30 seconds by using a spin coater (Fig. 2). After spinning, the samples were dried in an oven for 10 minutes to remove the organic residuals. To enhance the thickness of the NiO layer, the coating and drying procedures were conducted for a total of 10 cycles for each sample. The thickness of the NiO layer exhibits a dependence on pH, attributed to variations in nucleation and film formation processes. According to our findings, the maximum thickness was recorded at a pH of 11. This observation is likely a result of optimized nucleation and growth conditions at this specific pH level, which facilitates improved crystallization and densification of the NiO layer. After each coating, the samples were gradually annealed at 500 °C, 600 °C, and 700 °C for 1 hour under ambient conditions. Annealing at different temperatures helps optimize the crystalline structure of the NiO thin films. Moreover, the thermal treatment can influence parameters such as film density, porosity, and surface morphology. The gradual increase in temperature may facilitate the removal of residual solvents, enhance the interfacial bonding between the film and substrate, and promote the diffusion and rearrangement of atoms within the film. According to research conducted by Temesgen D. Desissa [10], annealing temperatures beyond 700°C (approximately 900°C) result in an XRD pattern indicating a stable interface without additional phases, albeit with a reduction in the 2-theta angle. However, it is noted that exceeding 700°C can lead to undesired effects such as film cracking and melting. Finally, the NiO thin films were formed with the thickness of 1.20 μm and 1.15 μm for the bottom and top layer respectively.

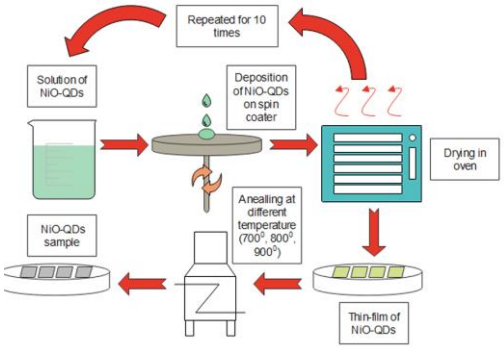

Fig. 2. Diagram of NiO deposition process repeated for 10 cycles and annealed at three different temperature.

2.5. Material Characterization of NiO

Analytical characterization techniques used in the investigation of NiO thin films are presented in detail in this section. X-ray powder diffraction (XRD) was used to determine the crystal structure and assess the crystallinity of NiO thin films. Moreover, Scanning Electron Microscope (SEM) was conducted to investigate the morphological surface of NiO films with different annealing temperatures. Fourier transform infrared spectroscopy (FTIR) analysis is employed to identify organic, inorganic, and polymeric compounds by scanning the samples with infrared light.

3. Result and Discussion

The pH value has always had a substantial effect on the outcomes for NiO material development through the chemical pathway. The pH of the synthesizing of the NiO precursor has a significant impact on the morphologies, crystal sizes, textural qualities, and microstructural content of the material. According to findings from the past, NiO that was manufactured under alkaline modes (with a pH of 8 or above) demonstrates superior stabilization performance in comparison to NiO that was manufactured under acidic modes [11]. As mentioned earlier, each pH level was categorized as the top layer (supernatant) and bottom layer (precipitate) (see Fig. 3). Moreover, the resulting NiO thin films were annealed at different annealing temperatures (500 °C, 600 °C, and 700 °C). The characterization of NiO were generally based on the structural, morphological, and element composition of NiO thin films. The evaluation of NiO thin films was carried out with the help of XRD, SEM, and FTIR. The characterization of their structures, along with their interfaces and defects, is essential to understand better how the synthesis pathways affect the quality and functional properties of the nanoparticles.

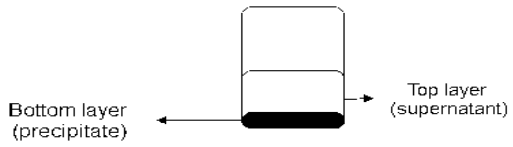

Fig. 3. NiO thin film categorized as the top layer (supernatant) and bottom layer (precipitate).

3.1. Structural Analysis of NiO

3.1.1. pH 9 of NiO

The data plot of Fig. 4 ((a)-(d) shows the XRD pattern for the bottom and top layer NiO thin films obtained at pH 9 as-deposited and three different annealing temperatures. As deposited bottom layer acts like amorphous material, with no peak (see Fig. 4 (a)). A similar pattern was observed in the XRD result published by Changyu Li and Shouxin Liu [12]. After the thermal treatment, the XRD pattern of the bottom layer NiO thin film at 500 ºC and 700 ºC exhibited sharp peaks at 37.2º corresponding to (1 1 1). Meanwhile, two wider bumps at 63.0º and 75.44º, which are respective to (2 2 0) and (3 1 1) planes are observed. Meanwhile, the annealing temperature of 600 ºC showed only one prominent peak at 62.84º, that is (2 2 0) diffraction of the cubic NiO diffraction planes (JCPDS card no. 70-1849). No secondary peaks are seen which, indicative of complete oxidation of the Ni and the absence of by-products of NiO production [8]–[10]. The XRD result of as-deposited top layer pH 9 showed one sharp diffraction peak occurring at 2θ~19.2° (0 0 1) and two broader diffraction peaks witnessed at 52.10º(1 0 2), and 70.10º(1 0 3) (see Fig. 4 (c)). These diffraction peaks are indexed to beta(β)-nickel(II) hydroxide (Ni(OH)2) (JCPDS:14-0117). Based on Fig. 4 (d), with increased temperature, NiO film at 500 ºC and 600 ºC shows three diffraction peaks at 37.0º, 62.84º and 75.44º which correspond to (1 1 1), (2 2 0), and (3 1 1). However, the top layer of NiO film at 700 ºC indicates a hollow peak. This might be due to NiO fully oxidizing at higher annealing temperatures, reducing the precursor solubility of the top layer at pH 9. At the annealing temperature of 500 ºC, the (2 2 0) peak exhibited increased intensity and sharper characteristics. Nevertheless, with a further rise in the annealing temperature, the (2 2 0) peak disappeared. A previous study by Melanie Budde et al [13] reported a reduction in the intensity of the (200) peak with increasing substrate temperature. The orientation of the films was believed to be contingent on the mobility of adatoms and clusters on the substrate [14], [15]. Films deposited at lower substrate temperatures displayed low atomic mobility, favoring the formation of a preferred orientation along the (2 2 0) direction. As the substrate temperature increased, adsorbed atoms gained additional thermal energy, enabling them to move to other preferred sites along the (2 2 0) direction. The crystallite size was determined by examining the orientation of the strong diffraction peak at (2 2 0). The study of the average size of integrated diffraction zones from XRD reflection broadening using the Scherrer formula (Eq. (1)) is the straightforward and most practical approach devised for nano-scale particle size estimation [16]. The crystallite size, D (nm), is related to the broadening of diffraction reflection patterns, described by an equation developed by P. Scherrer in 1918 [17],

$$D = \frac{0.9\lambda}{\beta \cos\theta} \quad (1)$$

where λ is the incident wavelength, β is the half-width of the diffraction peak quantified in radians, and θ is the peak location. Table 1 summarizes the effects of various annealing temperatures on the structural aspects of NiO thin films, comprising crystallite size, full width at half maximum (FWHM), and positional angle. The FWHM of the bottom and the top layer of NiO decreased from 2.2042º to 1.5744º and 1.8893º to 1.2595º correspondingly. This indicates the development of the NiO thin film at the bottom and top layer with rising annealing temperature, leading to larger crystallite sizes from 4.93 to 7.39 nm and 4.22 to 5.92 nm, respectively, as presented in Table 1. This also supports the ordering and structural improvements that occur during crystallization, in which, as the intensity is high, the FWHM is reduced to a minimal level [18]. The pH 9 NiO crystallite size increases as the annealed temperature increases using the Scherrer formula. As the temperature of annealing raised, the elements within the material are reorganized, generating crystal clusters. The crystal grain starts to expand, and the direction of development employs the emptiness among crystal clusters. When this growth direction consumes energy from the heat, the higher the annealing rate, the greater the crystal cluster's capability to utilize vacancies positions for expansion. Williamson– Hall (W-H) analysis was utilized to achieve a better understanding of the structural properties of the NiO materials. Williamson-Hall (W-H) evaluation is a generalized integral scopes approach that deconvolutes both size and strain-induced widening by evaluating peak widths as a function of 2θ [19]. The Williamson-Hall (W-H) formula (Eq. (2)) was applied to calculate the crystallite size and microstrain considering the width of the predominant XRD peak intensities.

$$\beta hkl = \left(\frac{0.9\lambda}{D}\right) + 4\varepsilon \sin\theta \quad (2)$$

In which D is the crystallite size (nm), λ is the radiation wavelengths (CuKα), βhkl is the FWHM of the principal peak intensity, ε refers to the microstrain that is caused to flaws inside the crystalline lattice, and θ is the diffraction angle. Fig. 5 ((a)-(b)) and Fig. 6 ((a)-(b)) represent the plots of β cos θ versus 4 sin θ for the bottom and top layers at the desired oriented peaks of the NiO samples. All the samples plotted showed the positive strain except for the bottom layer NiO annealed at 600 ºC and top layer NiO annealed at 700 ºC which showed a single diffraction peak

and hallow peak correspondingly, so there was no positive slope in the Williamson-Hall graph. From the W-H analysis, when the annealing temperature rises, the crystallite sizes of the bottom layer decrease. The findings indicate that the crystallite sizes of the pH 9 bottom layer derived from Scherrer's calculation are smaller compared to the Williamson Hall measurement. Meanwhile, W-H analysis for the top layer demonstrates that crystallite sizes decrease with increasing annealing temperature, confirming the same trend as Scherer's investigation. The crystallite size estimated by the W-H equation are greater than those determined by Scherrer's equation due to peak widening caused by microstrain measured by the W-H analysis (see Table 1). Applying Williamson-Hall evaluation and Scherrer's formula, a comparable pattern was detected in research focusing on NiO nanoparticles which showed a considerable variation in crystallite size [20], [21]. This variation could be explained as follows: microstrain might cause a higher widening of the diffraction peak, but the Scherrer equation emphasizes the complete width of the diffraction peak. In addition, as the annealing temperature increased, the microstrain (ε) of the bottom layer decreased from 1.399 to 0.94, whereas that for the top layer increased from 0.503 to 1.827. The microstrain arises from imperfections, defects, or distortions in the crystal lattice. These transitions may result in alterations in the crystal structure, affecting both crystallite size and microstrain. When raising the annealing temperature, the NiO thin film's stress is probably discharged, can lead to lattice distortions and the introduction of microstrain. The cumulative effect of the rise in microstrain can be utilized to explain the significant increase in the layering defect of films as the heating temperature increases [22].

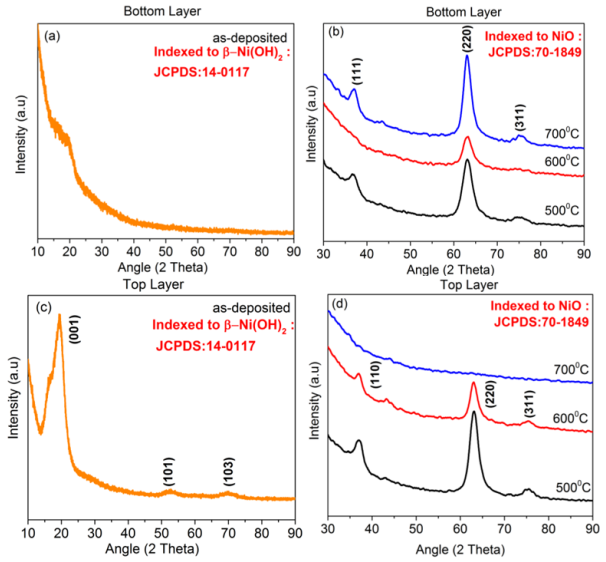

Fig. 4. X-ray diffraction patterns of pH 9 NiO film at (a) as-deposited bottom layer, (b) different temperature of the bottom layer, (c) as-deposited top layer, and (d) different temperature of the top layer.

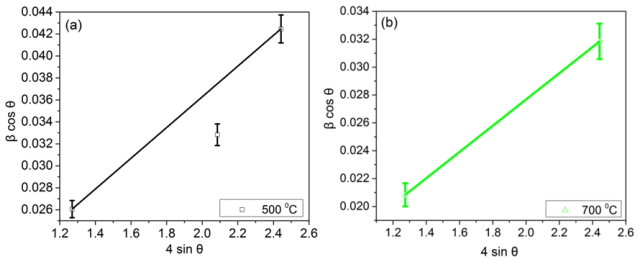

Fig. 5. The WH analysis for the bottom layer NiO thin film at pH 9 showed the positive strain at (a) 500 °C, and (b) 700 °C. Solid lines represent best-fitting lines, while error bars represent standard deviations. The slope was used to determine the strain, and the y-intercept was used to calculate the crystalline size.

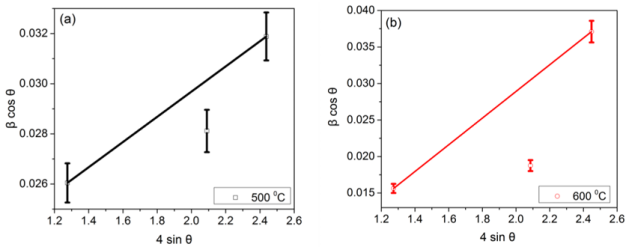

Fig. 6. The WH analysis for the top layer NiO thin film at pH 9 (a) 500 °C, and (b) 600 °C. Solid lines represent best-fitting lines, while error bars represent standard deviations.

3.1.2. pH 10 of NiO

The XRD pattern of the bottom and top layer NiO thin films at pH 10 for as-deposited and different annealing temperature are shown in Fig. 7 ((a)-(d)). Fig. 7 (a) shows a little increase in peak height at the 19.57°(0 0 1) XRD peak, which is indexed to the β-$Ni(OH)_2$. The rising of β-$Ni(OH)_2$ peak was observed in the bottom and top layer of as-deposited samples with increasing pH values from 9 to 10. This also represents the transformation of $Ni(OH)_2$ into Ni/NiO as the annealing temperature rises. Unexpectedly, no peak appears in the XRD pattern of the NiO film in the bottom layer heated to 500 °C. NiO thin film annealed at 600 °C showed diffraction peaks at 37.23°, 62.84°, and 75.44° while thin film annealed at 700 °C found only one peak at (2 2 0) plane. The diffraction peak at (2 2 0) plane of 600 °C is higher than at 700 °C annealing temperature. The absence of secondary peaks were observed, which means that all of the Ni had already been oxidized, and no NiO composition by-products were found [10], [23]. On the other hand, the XRD result of the as-deposited top layer pH 10 showed the diffraction peak occurring at (0 0 1) plane get sharper with increasing pH value (see Fig. 7 (c)). The top layer NiO film at annealing temperatures 500 °C, 600 °C, and 700 °C showed single diffraction peaks at 62.84° which correspond to (2 2 0). Equally, as for pH 9, the intense diffraction peak was observed at (2 2 0) to determine the crystallite size. Most of the pH 10 XRD results showed a single diffraction peak, so there was no positive slope in the Williamson-Hall graph which meant that the overall number of heterogeneous strains was very

small. The Williamson-Hall analysis only focused on the bottom layer that has been heated to 600 ºC. Scherrer's equation was also implemented to discover the crystallite size of pH 10 NiO. Based on Table 2, the crystallite size of pH 10 NiO using Scherrer's equation attained higher at a lower annealing temperature. In contrast to the behaviour of pH 9, the FWHM of the bottom and top layer pH 10 increased with enhancing thermal temperature. The XRD finding demonstrates that the larger FWHM of the NiO layers the smaller the crystallite size attained. Because the diffraction patterns widened, the crystallite size reduced. Consequently, as the pH level rises, the nanoparticles become smaller. Recently, Ritu Goel et.al [24], discussed that NiO nanoparticles with small crystallite size form a better thin film suitable for use as a HTL in solar cells. Fig. 7 reveals the W-H analysis for the bottom layer that had been annealed at 600 ºC. As determined by W-H interpretation, the crystallite size of 600 ºC annealed bottom layer NiO is significantly larger than the crystallite size determined using Scherrer's calculation. The microstrain in the NiO thin film is mainly responsible for this, as was discussed earlier. Scherrer's formula and W-H analysis provide independent estimates of the crystallite size of NiO nanoparticles [21].

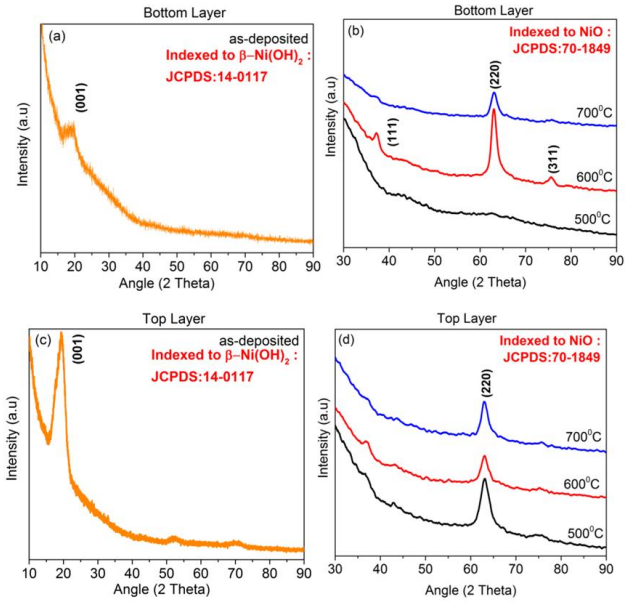

Fig. 7. X-ray diffraction patterns for pH value of 10 NiO film at (a) as-deposited bottom layer, (b) different temperature of the bottom layer, (c) as-deposited top layer, and (d) different temperature of the top layer.

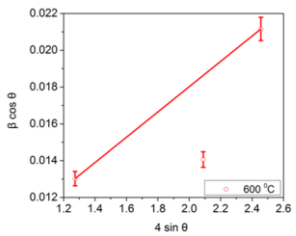

Fig. 8. The WH analysis for the bottom layer NiO thin film of pH 10 annealed at 600 ºC. Solid lines represent best-fitting lines, while error bars represent standard deviations obtained from Origin software.

3.1.3. pH 11 of NiO

The XRD patterns for the bottom and top layer NiO prepared at pH 11 are shown in Fig. 9 ((a)-(d)). As displayed in Fig. 9 (a), all four diffraction peaks of the as-deposited bottom layer can be readily indexed to β-$Ni(OH)_2$, corresponding to JCPDS:14-0117 without any impurity phase. Subsequently, the structure of the β-$Ni(OH)_2$, as evidenced by the presence of strong diffraction peaks at (0 0 1) plane. The appearance of diffraction peaks that are particularly broad and intense suggests that the β-$Ni(OH)_2$ nanoparticles are generally iso-axial and effectively dispersed throughout the nanoparticles [21]. The XRD pattern depicted in Fig. 9 (a) within the angle range of 30-50º reveals a slight amorphous behavior. This behavior is notable and is attributed to the material's exposure to air or an alkaline solution [25]. Additionally, the XRD pattern of the as-deposited bottom layer sample exhibits a minor hump at 38.7º, signifying the inferior crystallinity of the β-$Ni(OH)_2$ phase. On the other hand, as the annealing temperature increased from 500 ºC to 700 ºC, a more diffraction peak of NiO was detected as compared to pH 9 and 10. However, the diffraction peak of (2 0 0) and (3 1 1) heated at 500 ºC and 600 ºC slightly broader in contrast to thin films at 700 ºC (see Fig. 9 (b)). A narrow peak indicates a highly organized region within the film on the atomic scale. When the annealing temperature increases, the narrow peak appears and the wide peak expands [26]. These two characteristics indicate that decreasing the temperature leads to a rise in the number of flaws in the film, which can eventually lead to a larger mosaicity, which may have a significant effect on the NiO thin film's electrical properties. Notably, the XRD data of the bottom layer NiO at pH 11 display a prominent diffraction peak with increasing annealing temperature, in contrast to the XRD patterns of the bottom layer NiO at pH 9 and pH 10. The XRD pattern of β-$Ni(OH)_2$ structure was found in the top layer pH 11 NiO (see Fig. 9 (c)). The peak intensity at (0 0 1) plane was detected with higher intensity compared to the as deposited top layer of pH 9 and pH 10. Similar to the behavior observed in Fig. 9 (a), a subtle hump is noticeable at the (101) plane within the angle range of 30-50º in Fig. 9 (c). In this case, the top layer with a pH of 11 NiO exhibits minimal indications of crystalline NiO. The lack of NiO presence is linked to its conversion into β-$Ni(OH)_2$ during the potential cycling in KOH, which aligns with findings documented by Spela Trafela et al [25] that highlighting the impurities of crystallinity of the $Ni(OH)_2$ phase. Notably, the XRD data within the specified angle range does not reveal the presence of well-crystallized β-$Ni(OH)_2$ in both layers. Consequently, all significant peaks of NiO at 37.2º (1 1 1), 43.36º (2 0 0), 63.04º (2 2 0), and 75.51º (3 1 1) were observed in all three annealing temperature which is not achieved in previous pH level of the top layer (pH 9 and pH 10). As demonstrated in Fig. 9 (d), the diffraction peak at (2 2 0) top layer NiO thin film of pH 11 display strong and sharper peaks. Additionally, the sample heated at 500 ºC

to 600 ºC exhibited only a small proportion of diffraction planes which illustrated that the broad diffraction peak was indicative of the mosaicity appearance. Overall, the XRD graph illustrated that both layer consist of pure NiO crystalline structures with no discernible impurity peaks. Scherrer's formula and the W-H formula were applied to determine the crystallite size of pure β-$Ni(OH)_2$ and NiO at the highest intensity peak of the (0 0 1) plane and (2 2 0) plane, respectively. Based on the computation using Scherrer's formula, the as-deposited bottom layer pH 11 attained a crystallite size of 3.20 nm. With an increased annealing temperature to 500 ºC, the crystallite size emerges to 8.45 nm (see Table 3). After the temperature is set to 600 ºC and 700 ºC, the crystallite size decreases continuously. The crystallite size is inversely proportional to the FWHM, therefore the larger the FWHM the smaller is crystallite dimension. In parallel to the bottom layer result, the as-deposited top layer pH 11 also obtained decreasing crystallite size with increasing thermal temperature. As the annealing temperature rose from room temperature to 700 ºC, the FWHM peak values and individual peak intensities increased dramatically. This behaviour shows that the annealing approach makes the film more crystalline. In addition, the charge density is increased because smaller crystallites have a larger surface region and can interact with more ions. Fig. 10 ((a)-(b)) demonstrates the W-H analysis for the bottom layer NiO thin film at pH 11 with a solid line indicating the best fit. Based on the W-H analysis, Fig. 10 (a) shows the strain obtained at a negative slope. This can be explained by the fact that a negative slope indicates lattice compression [27]. The size of the crystallite was found to drop as the temperature increased. After thermal treatment, the incline has become positive. As a result, smaller crystallites and a smaller microstrain impact are detected when the XRD diffraction peaks are more substantial. Identically to Fig. 10 (a), the as-deposited top layer NiO at pH 11 also shows a negative slope due to the lattice compression as illustrated in Fig. 11 (a) [27], [28]. The increasing annealing temperature of all the top layer NiO indicates a positive slope, as seen in Fig. 11 (b), (c), and (d). The positive signal of the microstrain indicates a lattice expansion. Increasing the annealing temperature also activates relaxation mechanisms and reduces the strain level for both layer of NiO thin film. When the annealing temperature is lowered, the position of the NiO peak moves to the left. This shows that the NiO structure is expanding out of plane, which could be caused by a mismatch among the lattices of the film and the substrate. Films generated at lower temperatures exhibit more strain, proving that thermal energy plays a crucial part in the relaxing operation. It is possible that some of the misalignment strain will still be maintained in the film structure after annealing at low temperatures owing to the absence of a thermal driving force for surface diffusion. The crystallite size determined using the W-H plotting method is larger than that determined by the Scherrer's equation (Table 3). The Scherrer's equation computation of crystallite size differs significantly from the W-H formula calculation. This disparity can be rationalized as follows: the microstrain has the potential to cause a higher broadening of the diffraction peak, but the Scherrer equation takes into account the complete width of the diffraction peak in its calculations [29]. Scherrer equation and W-H analysis values for pH 11 NiO crystallite size exhibit a similar tendency with increasing thermal temperature. A good, straight line in the W-H plotting suggests that the sample has a consistent distribution of particle sizes and microstrain. The XRD pattern at pH 11 is substantially more successful than at lower pH levels owing to the existence of NiO diffraction peak intensity at all three temperatures, a sharp peak corresponding to an atomically long-range ordered region within the film, and none of the samples exhibiting an amorphous tendency. This is supported by the fact that the NiO diffraction peak acquired is more substantial when the precursor solution is at pH 11.

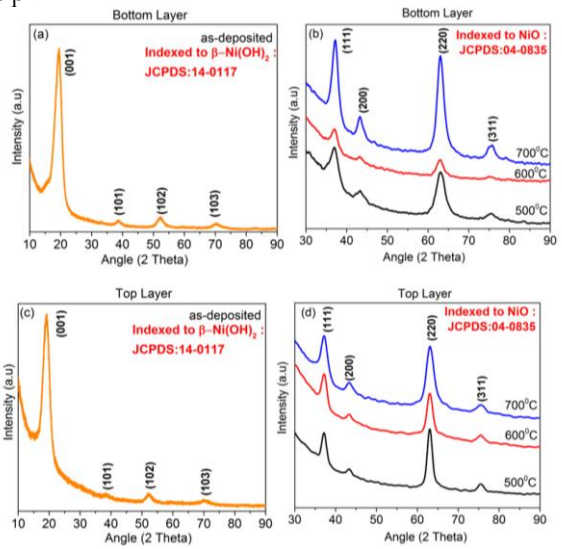

Fig. 9. X-ray diffraction patterns of pH 11 NiO film at (a) as-deposited bottom layer, (b) different temperature of bottom layer, (c) as-deposited top layer, and (d) different temperature of top layer.

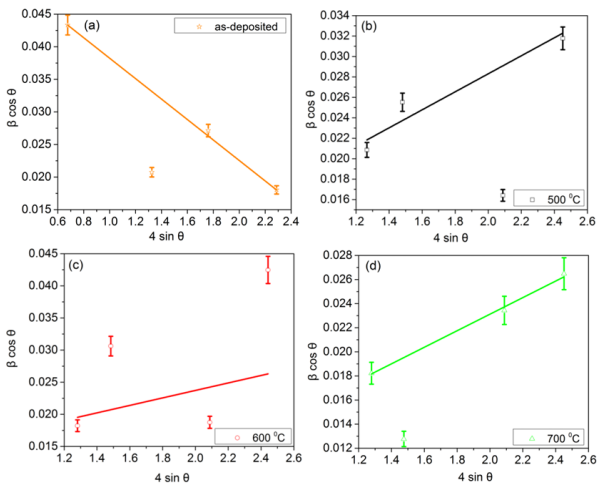

Fig. 10. The W-H analysis for the bottom layer NiO thin film at pH 11 (a) as-deposited (b)500 ºC, (c) 600 ºC and (d) 700 ºC. Solid lines represent best-fitting lines, while error bars represent standard deviations.

DOI:10.4186/ej.2025.29.4.23

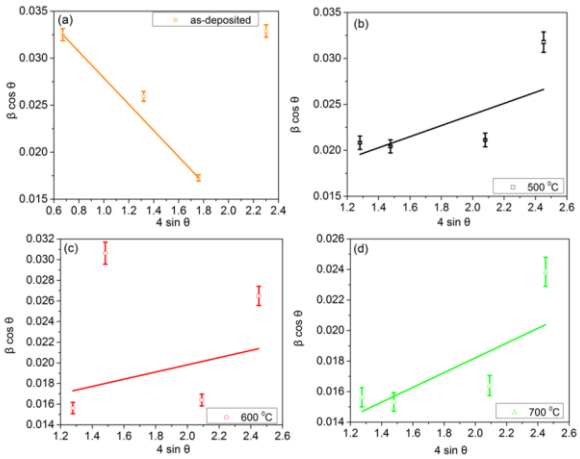

Fig. 11. The W-H analysis for the top layer NiO thin film at pH 11 (a) as-deposited, (b) 500 °C, (c) 600 °C and (d) 700 °C. Solid lines represent best-fitting lines, while error bars represent standard deviations.

3.1.4. pH 12 of NiO

The XRD results for the bottom and top layer NiO prepared at pH 12 is shown in Fig. 12 ((a)-(d)). The as-deposited bottom layer and as-deposited top layer of pH 12, act as amorphous material with no peak that is distinguished in the diffractograms (see Fig. 12 (a) and (c)). The low intensity and broadness peak were also observed as the pH of the NiO increased to 12. After heating the samples to 500 °C, low intensity of the diffraction peaks was obtained at the (1 1 1) and (2 2 0) diffraction planes. Surprisingly, a sharp peak was attained with a further increase of annealing temperature to 600 °C as seen in Fig. 12 (b). Four diffraction peaks of NiO were identified at 37.10°, 43.40°, 63.17° and 75.44° corresponding to the (1 1 1), (2 0 0), (2 2 0) and (3 1 1) diffraction plane. However, with more enhancement of temperature, low intense and broad diffraction peaks were observed at 700 °C, like the sample annealed at 500 °C. Likewise, top layer NiO with increasing annealing temperature demonstrates a much wider XRD diffraction peak at (2 2 0) plane. The XRD result of the top layer annealed at 600 °C displays a hollow peak. It is important to note that at this pH value, the presence of hollow peaks indicates that a portion of the sample becomes less saturated. The peak broadening also suggests that the lattice structure of NiO was poor at pH 12. Moreover, these broad peaks are evidence that the formed precipitates had a low crystallinity level. The crystallite sizes measured using the Scherrer formula and W-H analysis are presented in Table 4. Calculation based on the Scherrer formula shows that the crystallite size of the bottom layer is higher than in the top layer which can be confirmed by that the broadening of the diffraction peak results in smaller crystallite size. Even though there are some differences between both layers, the crystallite size keeps increasing with increasing annealing temperature. Moving on, crystallite size evaluated using W-H analysis show that bottom layer NiO annealed at 600 °C obtained a larger crystallite size of 14.94 nm. In comparison, samples at 500 °C and 700 °C produced smaller sizes with 7.86 nm and 6.58 nm, respectively. The increasing pH levels showed higher crystallinity, that described either by a high concentration of OH- functional group. Increasing the annealing temperature from 500 °C to 600 °C generated increasing crystallite, which also aligned with the positive slope demonstrated in Fig. 13 (a) and (b). Meanwhile, the reduction of FWHM and broadness of the peak intensity of the bottom layer for the sample heated at 700 °C, display negative strain which results in a lower crystallite size value (see Fig. 13 (c)). Compared to the previous sample of NiO annealed at 700 °C, only pH 12 show a negative slope owing to the poor crystallinity and much lattice compression. In general, enhancing the pH level of NiO (pH = 12) exhibited the diffraction peak wider and the intensity peak of NiO less visible. The characteristic peaks are much wider in intensity for all temperatures of annealed except the bottom layer heated at 600 °C. The lower intensity indicates that the products are of poor crystalline nature.

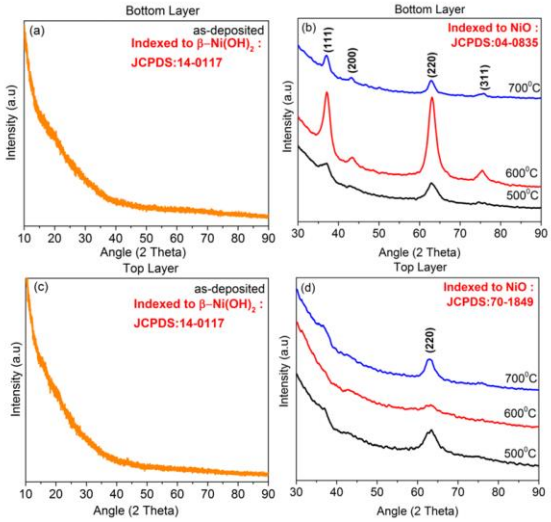

Fig. 12. X-ray diffraction patterns of pH 12 NiO film at (a) as-deposited bottom layer, (b) different temperature of the bottom layer, (c)as-deposited top layer, and (d) different temperature of the top layer.

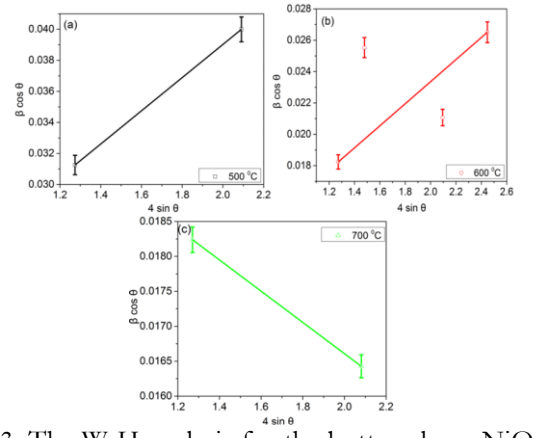

Fig. 13. The W-H analysis for the bottom layer NiO thin film at pH 12 (a)500 °C, (b)600 °C and (c) 700 °C. Solid lines represent best-fitting lines, while error bars represent standard deviations.

Table 1. The structural properties of the bottom and top layer NiO thin film at pH 9 with different annealing temperatures.

Temperature	*hkl*	2θ (deg)	θ (deg)	FWHW	[a]Crystallite Size (nm)	c x 10^2(nm)	[b]Crystallite Size (nm)	ε x 10^2
Bottom Layer								
500 °C	2 2 0	62.84	31.42	2.2042	4.22	0.831	16.68	1.399
600 °C	2 2 0	63.03	31.52	2.3040	4.04	-	-	-
700 °C	2 2 0	62.99	31.50	1.5744	5.92	0.884	15.68	0.94
Top Layer								
500 °C	2 2 0	63.00	31.50	1.8893	4.93	1.963	7.06	0.503
600 °C	2 2 0	62.85	31.43	1.2595	7.39	0.763	18.17	1.827
700 °C	No peak were detected							

Table 2. The structural properties of the bottom and top layer NiO thin film at pH 10 with different annealing temperatures.

Temperature	*hkl*	2θ (deg)	θ (deg)	FWHW	[a]Crystallite Size (nm)	c x 10^2(nm)	[b]Crystallite Size (nm)	ε x 10^2
Bottom Layer								
500 °C	No peak was detected							
600 °C	2 2 0	62.97	31.49	0.9446	9.86	-	-	-
700 °C	2 2 0	63.02	31.51	1.3440	6.93	-	-	-
Top Layer								
500 °C	2 2 0	63.10	31.55	1.1520	8.09	-	-	-
600 °C	2 2 0	63.07	31.54	1.3440	6.93	1.07	32.40	0.385
700 °C	2 2 0	62.87	31.44	1.3440	6.92	-	-	-

Table 3. The structural properties of the bottom and top layer NiO thin film at pH 11 with different annealing temperatures.

Temperature	*hkl*	2θ (deg)	θ (deg)	FWHW	[a]Crystallite Size (nm)	c x 10^2 (nm)	[b]Crystallite Size (nm)	ε x 10^2
Bottom Layer								
As-deposited	001	19.46	9.73	2.519	3.20	5.39	2.57	-1.57
500 ºC	2 2 0	62.95	31.56	1.1021	8.45	0.59	23.46	0.94
600 ºC	2 2 0	62.91	31.52	1.2595	7.39	0.67	20.73	0.80
700 ºC	2 2 0	62.93	31.52	1.5744	5.91	0.94	14.76	0.69
Top Layer								
As-deposited	001	19.32	9.66	1.8893	4.26	4.19	3.31	-1.40
500 ºC	2 2 0	62.66	31.33	1.1021	8.45	0.714	19.42	0.99
600 ºC	2 2 0	63.04	31.55	1.417	6.57	0.911	15.22	0.68
700 ºC	2 2 0	63.04	31.51	1.8444	5.05	0.008	13.17	0.59

Table 4. The structural properties of the bottom and top layer NiO thin film at pH 12 with different annealing temperatures.

Temperature	*hkl*	2θ (deg)	θ (deg)	FWHW	[a]Crystallite Size (nm)	c x 10^2 (nm)	[b]Crystallite Size (nm)	ε x 10^2
Bottom Layer								
500 ºC	2 2 0	63.02	31.51	2.688	3.47	1.76	7.86	1.070
600 ºC	2 2 0	63.17	31.59	1.417	6.58	0.928	14.94	0.704
700 ºC	2 2 0	62.69	31.35	1.1021	8.44	2.108	6.58	-0.224
Top Layer								
500 ºC	2 2 0	63.7	31.85	3.072	3.04	-	-	-
700 ºC	2 2 0	62.97	31.49	1.92	4.85	-	-	-

[a] *From Scherrer's formula*
[b] *From Williamson-Hall (WH) formula*

3.2. Morphology Analysis of NiO

The Scanning Electron Microscope (SEM) is a flexible, high-tech equipment commonly used to investigate the surface features of materials. The samples were treated with high-energy rays in a SEM and the emitted electrons/X-rays are examined [30], [31]. These electrons and X-rays provide details concerning a material's topography, structure, composition, arrangement of grains, crystallographic characteristics, etc. SEM is non-destructive, as the production of X-rays does not result in a loss of specimen volume; thus, the particular material can be analyzed multiple times [32], [33]. In this study, the morphological details of NiO for all pH levels were analyzed by SEM technique. SEM images of both layer (bottom and top) for as-deposited and annealed samples were obtained at a scale of 1 μm. Fig. 14 (a) and (b) shows the colour changes of NiO thin film for as-deposited and three different annealing temperatures that happen in all pH levels. Fig. 14 (a) and (b) displays the bottom and top layer NiO thin films, which were initially a bright green colour after being deposited on glass and getting darkened significantly throughout the annealing process. This colour change of NiO thin film is a good agreement with previous observations (Renaud et al., 2013) and could be due to nickel vacancies or interfacial oxygen defects. The transformation of NiO from dull green to dark brown may be due to the presence of Ni vacancies (point deficiencies) [34]. Besides that, the oxidation process of Ni^{2+} to Ni^{3+} caused a deep brown colouration of the film (Subramanian et al., 2008). NiO thin films change to a bleach condition as the annealing temperature is increased. According to Sun et.al [35], this is consistent with the removal of Ni metal in the Earth's crust. According to another report [36], bleaching occurs in NiO films because OH ions and electrons are continuously inserted and removed from the film. In this research, the XRD demonstrates that there are no other peaks of Ni, which is following the findings. The colour of the sample provides an approximate idea of the stoichiometry of NiO. Even small amounts of nickel with more significant valence states can change the colour of NiO a great deal. It has a broad range of electrochemical characteristics that depend on how it was made and on the defect formations that developed.

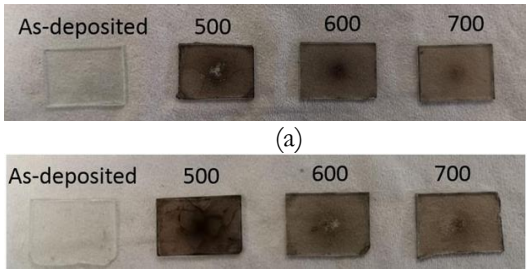

Fig. 14. NiO thin films' colour changing before and after annealing at 500 ºC, 600 ºC and 700 ºC for (a) the bottom layer and (b) the top layer.

3.2.1. pH 9 of NiO

Fig. 15 (a) and (b) depicts the SEM images of NiO thin film for the bottom and top layer, respectively. The surface morphologies of the bottom layer as-deposited thin films (Fig. 15 (b)) displays the particles arranged into an irregular structure with an agglomeration view. By increasing the annealing temperature to 500 ºC, the particles were observed with some agglomeration particles. The bottom layer of NiO thin film at 600 ºC and 700 ºC annealing temperature, indicating the Ni foam smooth surface consist of increased-sized Ni crystal grains. In Fig. 15 (b), the as-deposited top layer displays a smooth surface but with aggregation behavior. The sample of top layer NiO annealed at 500 ºC, was observed with black spots on the surface structures but free from pinholes. The films are seen to be more uniform, with a smoother and finer morphology, with film temperature increasing from 600 ºC to 700 ºC.

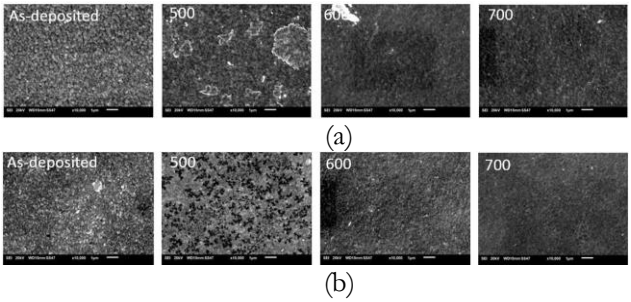

Fig. 15. The SEM images of NiO thin films at pH 9 as-deposited and annealed sample (500 ºC, 600 ºC and 700 ºC) for (a) bottom layer and (b) top layer

3.2.2. pH 10 of NiO

The morphology studies of pH 10 NiO thin film presents in Fig. 16 (a) and (b) for the bottom and top layers correspondingly. The SEM images of the as-deposited bottom (see Fig. 16 (a)) and the top layer (see Fig. 16 (b)) reveals the particles display aggregation behaviour. In Fig. 16 (a), the agglomeration size of the particles increased from 500 ºC to 700 ºC. This illustrates that the particles consist of irregular shapes. However, in Fig. 16 (b), NiO thin film at rising annealing temperature (from 500 ºC to 700 ºC) exhibits the particles size in a spherical structure with a slightly low uniformity surface and less agglomeration behaviour. The SEM measurements revealed that the bottom and top layers of pH 10 annealed and as-deposited NiO are free of cracks and pinholes.

3.2.3. pH 11 of NiO

The SEM characteristics of synthesized NiO at pH 11 for the bottom and the top layer are illustrated in Fig. 17 (a) and (b). The SEM images at the as-deposited bottom layer (Fig. 17 (a)) shows that the particles have a spherical shape with some degree of agglomeration. Randomly scattered grains of smaller size are seen when the annealing temperature increased. As compared to the

DOI:10.4186/ej.2025.29.4.23

surface area of the as-deposited NiO thin film, the surface area of the NiO thin film at three distinct annealing temperatures is much more uniform. Contrary to the as-deposited NiO thin film, the arrangement of particles is compact in the bottom layer annealed NiO thin film. Similarly, with as-deposited in Fig. 16 (a), as-deposited in Fig. 16 (b) showed some agglomeration of particles. The surface topography of the top layer of NiO film with increasing temperature exhibited a moderate uniform surface. A small agglomeration of particles observed at 500 ºC and further increment of thermal temperature from 600 ºC to 700 ºC shows flawless, and less uniform surface morphology. However, there were no presence of pinhole and cracks in the pH 11 sample. In general, NiO at pH 11 offers better coverage compared to pH 9 and 10, with less agglomeration of particles and a uniform surface.

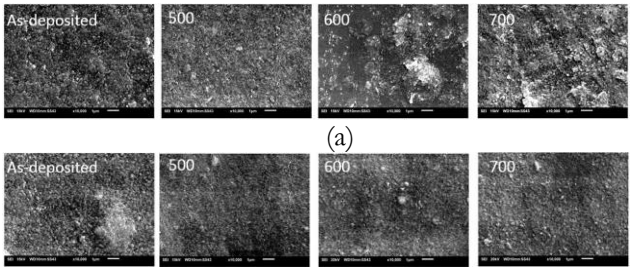

Fig. 16. The SEM images of NiO thin films at pH 10 as-deposited and annealed sample (500 ºC, 600 ºC and 700 ºC) for (a) bottom layer and (b) top layer

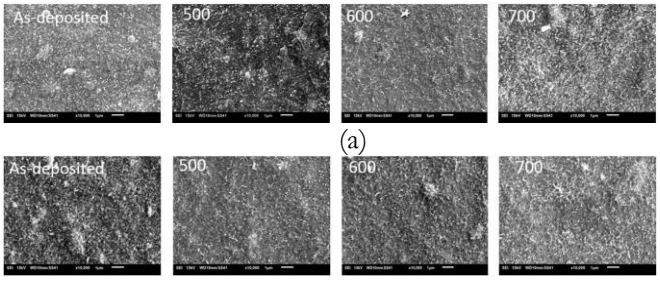

Fig. 17. The SEM images of NiO thin films at pH 11 as-deposited and annealed sample (500 ºC, 600 ºC and 700 ºC) for (a) bottom layer and (b) top layer

3.2.4. pH 12 of NiO

The result of surface morphological features of synthesized NiO at pH 12 at the bottom and top layer displays in Fig. 18 (a) and (b). The SEM micrograph for the as-deposited bottom layer show that the particles have a high degree of aggregation behavior. With the increase of annealing temperature, the flatness of the film morphology also gets higher which leads to low uniformity. The agglomeration of particles tends to reduce with rising temperature. In conjunction with Fig. 18 (a), the SEM image of the as-deposited top layer in Fig. 18 (b) exhibits a non-uniform surface and irregular shape of particles. In parallel to the bottom layer at 500 ºC, the growth of particles and poor surface flatness were observed at the top layer at 500 ºC. The film morphology of the top layer NiO at 600 ºC appeared with minor black dots on the film growth surface. The top layer of NiO thin film at 700 ºC shows less uniform surface morphology. With further increasing pH level (> pH 11) the SEM image of NiO showed a non-uniform surface.

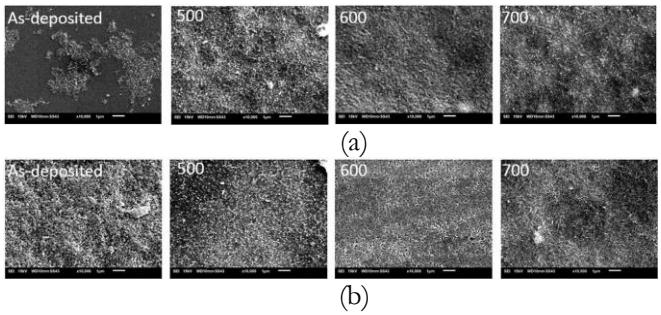

Fig. 18. The SEM images of NiO thin films at pH 12 as-deposited and annealed sample (500 ºC, 600 ºC and 700 ºC) for (a) bottom layer and (b) top layer.

3.3. Functional Groups of NiO

The Fourier transform infrared (FTIR) method is utilized to provide the radiation pattern of absorbance and greater conductivity in solids, liquids, and gases. It is employed to indicate distinct functional classifications. The sample transforms the received radiation into vibrational or rotational energy [37]. The output waveform at the analyser has a spectrum ranging from 4000 to 400 cm^{-1}. The FTIR spectra for different pH levels is shown in Fig. 19. The sample was tested as a dried green powder which is obtained from the final filtration of precursor samples of different pH solutions. The narrow and sharp peak at 3630 cm^{-1} and 3640 cm^{-1} corresponds to the stretching vibration (υO–H) of non-hydrogen bonded hydroxyl groups, which is characteristic of beta nickel hydroxide (β-$Ni(OH)_2$) [38]. A weak band near 1640 cm^{-1} produced by pH 12 assigned to H–O–H bending vibrations mode which was due to the absorption of water in the air when FTIR sample disks were prepared in the open air. The O–C=O symmetric and asymmetric stretching impulses, and the C–O stretching vibration, are referred to as the serrated absorption peaks in the region of 1000–1500 cm^{-1}, yet the amplitude of the band has lowered in pH 9,10, and 12, indicating that the ultrafine powers attempt to vigorously accumulate H_2O and CO_2 [39]. The C=C stretching mode of quinoid rings occurs around 1590 to 1550 cm^{-1}. The peak at 1380 cm^{-1} is probably due to the interaction of synthesized nanomaterial with potassium bromide (KBr) because FTIR was prepared with KBr powder [40]. The absorption band in the regions of 512cm^{-1}, 543cm^{-1}, and 600cm^{-1} were assigned to Ni– O stretching vibration mode [41]. The band appears at 490 cm^{-1}, 430 cm^{-1}, and 415 cm^{-1}, which is related to the Ni–O stretching vibration of nickel nitrate (NiO_6) octahedral in the cubic NiO structure, which shows the formation of the nanoparticle NiO [40], [42]. The shifting of the absorption band to a larger wave number or smaller wavelength indicates that the NiO sample is nanocrystalline, as verified by XRD data. This

shows that the FTIR spectrum data confirmed the formation of NiO nanoparticles.

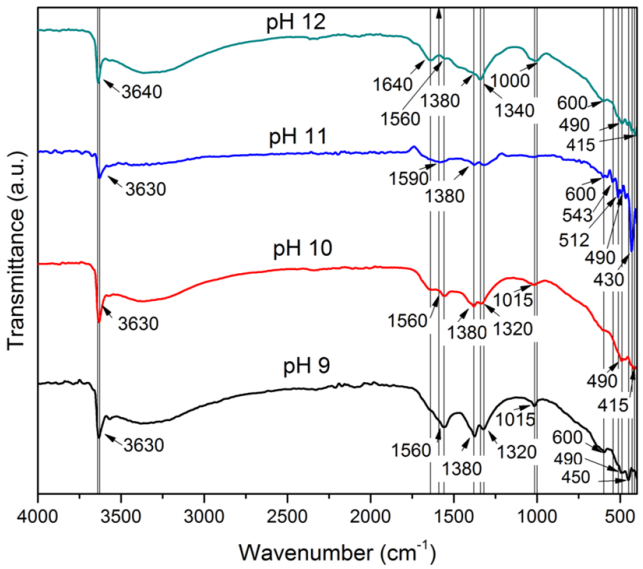

Fig. 19. FTIR spectrum of the NiO film at a different pH value (9 -12)

4. Conclusion

Overall, the performance of the NiO thin film at pH 11 show better and good properties based on the observation and analysis of characterization result obtained through XRD, SEM, and FTIR compared to other pH levels. In terms of structural analysis, almost all the prominent diffraction peaks of NiO were observed in pH 11 for each of the samples at both layer with more intense and sharper intensity. No hallow peaks are seen in the pH 11 NiO thin film. With the aid of Scherrer's and W-H formulas, the crystalline size was calculated. Both layer show decreasing crystalline size with increasing annealing temperature. Moreover, the study based on morphology analysis revealed that the surface of pH 11 was examined without any pinholes and black dots. The coverage was much better in pH 11 with less agglomeration of particles compared to other pH levels. According to the FTIR analysis, a strong absorption peak around 400cm-1 to 600cm-1, ascribed to the presence of NiO nanoparticle vibration, was observed in pH 11. Based on the characterization result, the performance of NiO-QDs at pH 11 were more suitable as HTL in PSC. This can be supported by the result found that the ideal temperature for the bottom and top layer NiO-QDs of pH 11 growth lies at 700 ºC, displays higher energy bandgap, reduces crystallite size, free pinholes and voids inside the film, least surface roughness, high dielectric constant, decrease strain level, and least amount nickel vacancies. This research work provided experimental validation to explain the theoretical knowledge about the electrical and optical properties of NiO-QDs as HTL. Besides that, the experimental results also demonstrate that NiO-QDs as HTL is a good alternative for solar cell materials through low-cost and simple processes.

Acknowledgement

This work was supported by the Ministry of Higher Education Malaysia and Technical University of Malaysia Melaka through the Fundamental Research Grant Scheme with Project No. PJP/2024/FTKEK/PERINTIS/SA0018 and the Kesidang Scholarship. The authors declare no conflict of interest.

References

[1] M. M. A. Moon, M. F. Rahman, J. Hossain, and A. B. M. Ismail, "Comparative study of the second generation a-Si: H, CdTe, and CIGS thin-film solar cells," *Adv. Mater. Res.*, vol. 1154, pp. 102–111, 2019.

[2] I. Hussain, H. P. Tran, J. Jaksik, J. Moore, N. Islam, and M. J. Uddin, "Functional materials, device architecture, and flexibility of perovskite solar cell," *Emergent Mater.*, vol. 1, pp. 133–154, 2018.

[3] T. Ibn-Mohammed *et al.*, "Perovskite solar cells: An integrated hybrid lifecycle assessment and review in comparison with other photovoltaic technologies," *Renew. Sustain. Energy Rev.*, vol. 80, pp. 1321–1344, 2017, doi: https://doi.org/10.1016/j.rser.2017.05.095.

[4] M. I. Hossain *et al.*, "Electrical and optical properties of nickel-oxide films for efficient perovskite solar cells," *Small Methods*, vol. 4, no. 9, p. 2000454, 2020.

[5] A. C. Nkele *et al.*, "The use of nickel oxide as a hole transport material in perovskite solar cell configuration: Achieving a high performance and stable device," *Int. J. Energy Res.*, vol. 44, no. 13, pp. 9839–9863, 2020.

[6] Q. Wang, Z. Lin, J. Su, Z. Hu, J. Chang, and Y. Hao, "Recent progress of inorganic hole transport materials for efficient and stable perovskite solar cells," *Nano Sel.*, vol. 2, no. 6, pp. 1055–1080, 2021.

[7] S. Muniandy *et al.*, "The effect of thickness variations on the performance of different lead-free perovskite solar cells using GPVDM," 2022.

[8] S. Muniandy, M. I. Bin Idris, Z. A. F. B. M. Napiah, and M. Rashid, "The effect of pH level and annealing temperature on NiO thin films as hole transport material in inverted perovskite solar cells," in *2022 IEEE International Conference on Semiconductor Electronics (ICSE)*, 2022, pp. 13–16.

[9] S. Muniandy *et al.*, "The effect of different precursor solutions on the structural, morphological, and optical properties of nickel oxide as an efficient hole transport layer for perovskite solar cells," *Pertanika J. Sci. Technol.*, vol. 31, no. 4, 2023.

[10] T. D. Desissa, "NiO--ZnO based junction interface as high-temperature contact materials," *Ceram. Int.*, vol. 47, no. 6, pp. 8053–8059, 2021.

[11] E. Arciga-Duran, Y. Meas, J. J. Pérez-Bueno, J. C. Ballesteros, and G. Trejo, "Effect of oxygen vacancies in electrodeposited NiO towards the oxygen evolution reaction: role of Ni-Glycine complexes," *Electrochim. Acta*, vol. 268, pp. 49–58,

2018.
[12] C. Li and S. Liu, "Preparation and characterization of $Ni(OH)_2$ and NiO mesoporous nanosheets," *J. Nanomater.*, vol. 2012, 2012.
[13] M. Budde *et al.*, "Structural, optical, and electrical properties of unintentionally doped NiO layers grown on MgO by plasma-assisted molecular beam epitaxy," *J. Appl. Phys.*, vol. 123, no. 19, 2018.
[14] Y. S. Jung and S. S. Lee, "Development of indium tin oxide film texture during DC magnetron sputtering deposition," *J. Cryst. Growth*, vol. 259, no. 4, pp. 343–351, 2003.
[15] A. Madhavi, C. S. Reddy, N. V Ravindra, P. Lokeshand, and P. S. Reddy, "Effect of substrate temperature on the structural, optical and electrical properties of electron beam evaporated NiO thin films," *Int. J. Adv. Res. Phys. Sci.*, vol. 1, pp. 16–20, 2014.
[16] A. S. Vorokh, "Scherrer formula: Estimation of error in determining small nanoparticle size," *Наносистемы: физика, химия, математика*, vol. 9, no. 3, pp. 364–369, 2018.
[17] P. Scherrer, "Bestimmung dergrosse und der inneren struktur yon kolloiteilchen mittels," *Gott. Nachr Math. Phys*, vol. 2, pp. 98–100, 1918.
[18] S. Y. Takko, B. D. E. Amin, and C. I. Y. I. J. Shekarau, "Crystallinity, amorphousity and characterization of synthesized Sb_2O_3, BaO and NiO Nanoparticles and Nanocomposites," *Int. J. Innovat. Sci. Res. Technol.*, vol. 6, no. 11, pp. 822-831, 2021.
[19] V. D. Mote, Y. Purushotham, and B. N. Dole, "Williamson-Hall analysis in estimation of lattice strain in nanometer-sized ZnO particles," *J. Theor. Appl. Phys.*, vol. 6, no. 1, pp. 1–8, 2012.
[20] N. S. Gonçalves, J. A. Carvalho, Z. M. Lima, and J. M. Sasaki, "Size-strain study of NiO nanoparticles by X-ray powder diffraction line broadening," *Mater. Lett.*, vol. 72, pp. 36–38, 2012.
[21] A. Singh *et al.*, "Structurally and morphologically engineered single-pot biogenic synthesis of NiO nanoparticles with enhanced photocatalytic and antimicrobial activities," *J. Clean. Prod.*, vol. 343, p. 131026, 2022.
[22] M. S. Jamal *et al.*, "Effects of growth temperature on the photovoltaic properties of RF sputtered undoped NiO thin films," *Results Phys.*, vol. 14, p. 102360, 2019.
[23] S. Muniandy, M. I. Bin Idris, Z. A. F. B. M. Napiah, H. H. M. Yusof, S. A. M. Chachuli, and M. Rashid, "An investigation on NiO for hole transport material in perovskite solar cells," in *2021 IEEE Regional Symposium on Micro and Nanoelectronics (RSM)*, 2021, pp. 112–115. doi: 10.1109/RSM52397.2021.9511573.
[24] R. Goel, R. Jha, and C. Ravikant, "Investigating the structural, electrochemical, and optical properties of p-type spherical nickel oxide (NiO) nanoparticles," *J. Phys. Chem. Solids*, vol. 144, p. 109488, 2020.
[25] Š. Trafela, J. Zavašnik, S. Šturm, and K. Ž. Rožman, "Formation of a $Ni(OH)_2$/NiOOH active redox couple on nickel nanowires for formaldehyde detection in alkaline media," *Electrochim. Acta*, vol. 309, pp. 346–353, 2019.
[26] A. Kashir, H.-W. Jeong, G. Lee, P. Mikheenko, and Y. H. Jeong, "Dielectric properties of strained NiO thin films," *arXiv Prepr. arXiv1904.07564*, 2019.
[27] M. Rabiei, A. Palevicius, A. Monshi, S. Nasiri, A. Vilkauskas, and G. Janusas, "Comparing methods for calculating nano crystal size of natural hydroxyapatite using X-ray diffraction," *Nanomaterials*, vol. 10, no. 9, p. 1627, 2020.
[28] Adiba, V. Pandey, S. Munjal, and T. Ahmad, "NiO nanoparticles: Phase purification and strain analysis," in *AIP Conference Proceedings*, 2021, p. 20121.
[29] H. M. Mohaideen, S. S. Fareed, and B. Natarajan, "Role of calcination temperatures on the structural and optical properties of NiO nanoparticles," *Surf. Rev. Lett.*, vol. 26, no. 08, p. 1950043, 2019.
[30] M. K. Jung and J. Y. Mun, "Sample preparation and imaging of exosomes by transmission electron microscopy," *JoVE (Journal Vis. Exp.*, no. 131, p. e56482, 2018.
[31] A. Ul-Hamid, *A Beginners' Guide to Scanning Electron Microscopy*, vol. 1. Springer, 2018.
[32] K. Akhtar, S. A. Khan, S. B. Khan, and A. M. Asiri, "Scanning electron microscopy: Principle and applications in nanomaterials characterization," in *Handbook of Materials Characterization*. Springer, 2018, pp. 113–145.
[33] D. Bazin *et al.*, "Scanning electron microscopy—A powerful imaging technique for the clinician," *Comptes Rendus. Chim.*, vol. 25, no. S1, pp. 37–60, 2022.
[34] A. Renaud *et al.*, "Origin of the black color of NiO used as photocathode in p-type dye-sensitized solar cells," *J. Phys. Chem. C*, vol. 117, no. 44, pp. 22478–22483, 2013.
[35] D.-L. Sun, B.-W. Zhao, J.-B. Liu, H. Wang, and H. Yan, "Application of nickel oxide nanoparticles in electrochromic materials," *Ionics (Kiel).*, vol. 23, no. 6, pp. 1509–1515, 2017.
[36] B. Subramanian *et al.*, "Optoelectronic and electrochemical properties of nickel oxide (NiO) films deposited by DC reactive magnetron sputtering," *Phys. B Condens. Matter*, vol. 403, no. 21–22, pp. 4104–4110, 2008.
[37] D. Titus, E. J. J. Samuel, and S. M. Roopan, "Nanoparticle characterization techniques," in *Green Synthesis, Characterization and Applications of Nanoparticles*. Elsevier, 2019, pp. 303–319.
[38] X. H. Xia, J. P. Tu, J. Zhang, X. L. Wang, W. K. Zhang, and H. Huang, "Electrochromic properties of porous NiO thin films prepared by a chemical bath deposition," *Sol. Energy Mater. Sol. Cells*, vol. 92, no. 6, pp. 628–633, 2008.
[39] M. Hashem *et al.*, "Fabrication and characterization of semiconductor nickel oxide (NiO) nanoparticles manufactured using a facile thermal treatment," *Results Phys.*, vol. 6, pp. 1024–1030, 2016.
[40] A. G. Al-Sehemi, A. S. Al-Shihri, A. Kalam, G. Du,

and T. Ahmad, "Microwave synthesis, optical properties and surface area studies of NiO nanoparticles," *J. Mol. Struct.*, vol. 1058, pp. 56–61, 2014.

[41] N. A. Jawad and K. H. Hassan, "Structural characterization of NiO nanoparticles prepared by green chemistry synthesis using *Arundo donaxi* leaves extract," in *Journal of Physics: Conference Series*, 2021, p. 12007.

[42] P. K. Sharma, M. K. Singh, G. D. Sharma, and A. Agrawal, "NiO nanoparticles: Facile route synthesis, characterization and potential towards third generation solar cell," *Mater. Today Proc.*, vol. 43, pp. 3061–3065, 2021.

S.Muniandy was born in Johor, Malaysia on May 6. She received her Bachelor's and Master's degrees in Electronic Engineering from Universiti Teknikal Malaysia Melaka (UTeM) in 2021 and 2024, respectively, and is currently pursuing her Ph.D. in the same field at UTeM. From 2021 to 2024, she was a Graduate Research Assistant at UTeM with Micro & Nano Electronics Research Group (MiNE) Laboratory. Her research focuses on solar energy, sustainable environments, energy applications, thin films, and hole-transporting layers, with several journal and conference papers related to perovskite solar cells. A member of IEEE, she has received notable accolades, including the Best Student Presenter Award at the 2023 IEEE RSM Conference and the 1st Runner-Up award in the University-level 3-Minute Thesis competition.

M.I.B. Idris was born in Johor, Malaysia on December, 9. He is a Senior Lecturer at the Faculty of Electronic and Computer Technology Engineering, Universiti Teknikal Malaysia Melaka (UTeM). He earned his Ph.D. in 2018 from Newcastle University, his Master's degree from Universiti Kebangsaan Malaysia (UKM) in 2012, and his Bachelor's degree from Hiroshima University in 2010. He specializes in electronic and computer engineering, with expertise in VLSI design, microprocessor technology, and artificial intelligence. He has taught various undergraduate and postgraduate courses, including Computer Architecture, Logic Circuits, and Sensor Technology. His research encompasses solar cells, nanomaterials, energy-efficient systems, and advanced sensor technologies. His innovative work has led to publications in high-impact journals and conference proceedings, and he has contributed to intellectual property development, including patents for IoT-enabled systems and thin-film fabrication methods. He has received numerous awards, including international gold medals for his work on flexible electronics and thin-film technologies.